nature photonics

ARTICLES

https://doi.org/10.1038/s41566-021-00810-1

Tunable quantum interference using a topological source of indistinguishable photon pairs

Sunil Mittal[1,2,5]✉, Venkata Vikram Orre[1,2,5], Elizabeth A. Goldschmidt[3] and Mohammad Hafezi[1,2,4]

Sources of quantum light, in particular correlated photon pairs that are indistinguishable for all degrees of freedom, are the fundamental resource for photonic quantum computation and simulation. Although such sources have been recently realized using integrated photonics, they offer limited ability to tune the spectral and temporal correlations between generated photons because they rely on a single component, such as a ring resonator. Here, we demonstrate a tunable source of indistinguishable photon pairs using dual-pump spontaneous four-wave mixing in a topological system comprising a two-dimensional array of resonators. We exploit the linear dispersion of the topological edge states to tune the spectral bandwidth (by about 3.5×), and thereby, to tune quantum interference between generated photons by tuning the two pump frequencies. We demonstrate energy–time entanglement and, using numerical simulations, confirm the topological robustness of our source. Our results could lead to tunable, frequency-multiplexed quantum light sources for photonic quantum technologies.

Spurred by the possibility of realizing continuous-variable photonic quantum computation[1], and protocols like Gaussian boson sampling[2] that hold near-term promise for quantum simulations and various graph-theory problems, nanophotonic systems have emerged as a natural platform with which to generate indistinguishable correlated photon pairs and, in the strong nonlinearity regime, single-mode squeezed light[3–7]. Most on-chip sources of indistinguishable photon pairs rely on dual-pump spontaneous four-wave mixing (SFWM), a third-order nonlinear process, in silicon or silicon-nitride waveguides and ring resonators[3–7]. In this process, two pump photons at different frequencies annihilate and create two frequency-degenerate photons, called the signal and the idler. The tight mode confinement in nanophotonic waveguides and the use of a ring resonator greatly enhance the strength of SFWM interactions, leading to an enhancement in pair-generation rates and eventually to the realization of on-chip sources of squeezed light[6–9]. Extensions of these simple single-element systems to multi-mode, multi-resonator systems can enable tunability and multiplexing of various spectral or temporal modes, and hence a substantial reduction in physical resources[10–12]. However, such extensions have so far remained elusive.

At the same time, the influx of ideas derived from the physics of topological insulators has led to a new paradigm of photonic devices that use arrays of coupled waveguides or resonators to achieve unprecedented control over the flow of photons[13–21]. More specifically, edge states, the hallmark of topological systems, exhibit unique features such as unidirectional (or helical) flow of photons confined to the boundaries of a system, linear dispersion, and an inherent robustness against disorders. Photonic edge states have now been used to realize robust optical delay lines[18,20,22], lasers[23–25], optical fibres[26], and reconfigurable pathways on chips[27,28]. More recently, topological edge states have been exploited in quantum photonic devices, to realize chiral quantum-optic interfaces between quantum dots and photonic crystals[29], topological beamsplitters for quantum interference of photons[30], quantum walks of correlated photon pairs[31], and also topological sources of quantum light[32,33]. In particular, in ref. [32] we implemented a topological source of distinguishable photon pairs using single-pump SFWM in a two-dimensional (2D) lattice of coupled ring resonators.

Here we report spectrally engineered generation of indistinguishable photon pairs via dual-pump SFWM in a 2D lattice of coupled ring resonators. This lattice realizes the anomalous quantum Hall model for photons and exhibits topological edge states[20,34–36]. We show that the linear dispersion of the edge states results in phase-matched generation of photon pairs throughout the edge band and thus allows us to tune the spectral–temporal bandwidth of photon pairs by tuning the input pump frequencies in the edge band. To show that the generated photon pairs are indeed indistinguishable, we use the fact that our system is time-reversal symmetric and therefore supports two pseudo-spins with corresponding edge states that circulate around the lattice in opposite directions (Fig. 1). We use these counter-propagating edge states to create path-entanglement in a Sagnac interferometer and thereby, deterministically split the indistinguishable photon pairs[4,37]. We then demonstrate Hong–Ou–Mandel (HOM) interference between split photons, which unequivocally establishes their indistinguishability. Furthermore, we show that the tunability of the spectral bandwidth of our source manifests in the temporal width of the HOM interference dip. Finally, we demonstrate that the generated photon pairs are energy–time entangled[38], as expected for a SFWM process with a continuous-wave pump, and that our source is robust against fabrication disorders. In contrast to our previous realization of the topological source of distinguishable photon pairs where we used the integer quantum Hall model (ref. [32]), here we use the anomalous quantum Hall model. The presence of next-nearest-neighbour couplings in this model yields an edge band that is twice the width of that in the integer quantum Hall model[35,36]. We exploit this substantially wider edge band to tune our source in a larger range. Our results could lead to the realization of on-chip, topologically robust and spectrally engineered sources of squeezed light for applications

[1]Joint Quantum Institute, NIST/University of Maryland, College Park, MD, USA. [2]Department of Electrical and Computer Engineering and IREAP, University of Maryland, College Park, MD, USA. [3]Department of Physics, University of Illinois at Urbana - Champaign, Urbana, IL, USA. [4]Department of Physics, University of Maryland, College Park, MD, USA. [5]These authors contributed equally: Sunil Mittal, Venkata Vikram Orre. ✉e-mail: mittals@umd.edu

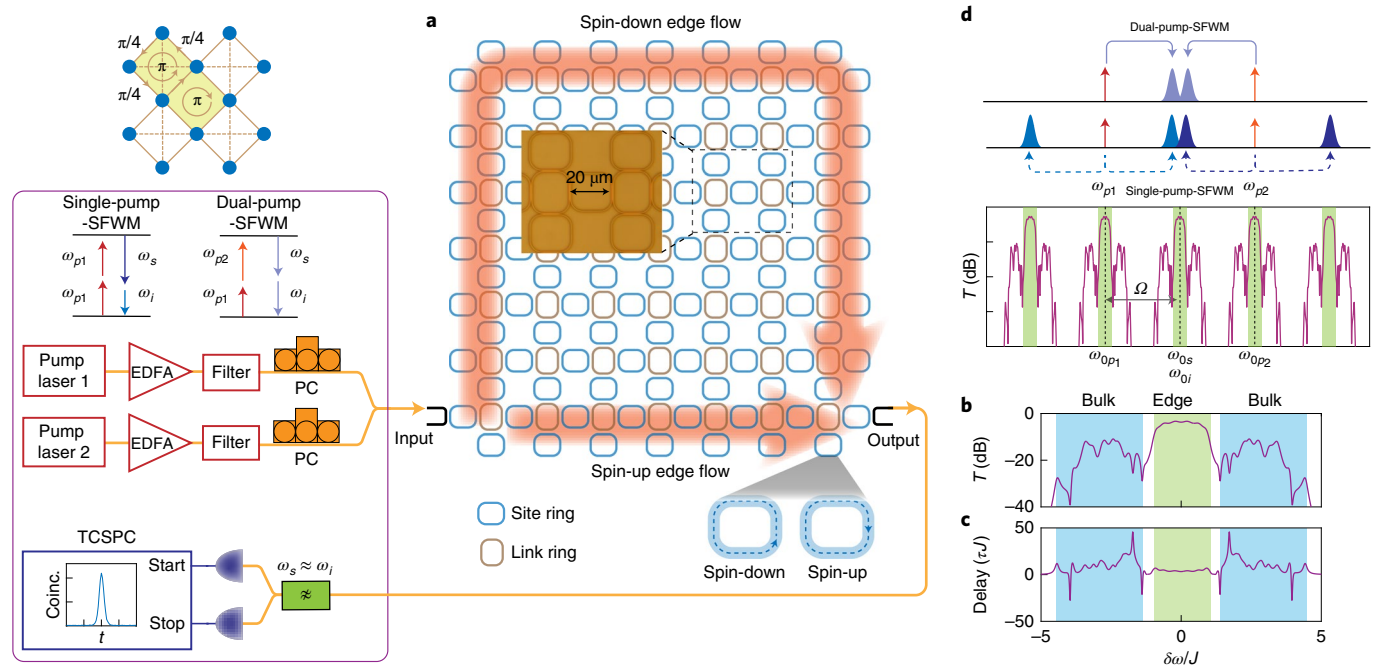

Fig. 1 | Schematic of the experimental setup. a, Schematic of the 2D array of silicon ring resonators that simulates the anomalous quantum-Hall model for photons. The link rings (shaded brown) couple nearest and next-nearest-neighbour site rings (blue), with hopping phases as shown in the top-left inset. The lattice supports two pseudo-spins (up and down), with corresponding edge states travelling in opposite directions. A given pseudo-spin can be excited in the system by appropriately selecting the input port[20,36]. **b**,**c**, Simulated transmission (T) and delay spectra of the device showing edge and bulk bands. The spectrum repeats after every free-spectral range (Ω). **d**, Pumping scheme to generate indistinguishable photon pairs via dual-pump SFWM. The lattice is pumped using two continuous-wave lasers, in different free-spectral ranges centred at ω_{0p_1} and ω_{0p_1}. At the output, we use tunable filters (centred around $\omega_s \approx \omega_i$) to suppress pump photons, two superconducting nanowire detectors and a time-correlated single photon counter (TCSPC) to perform time-resolved coincidence (Coinc.) detection. This measurement scheme allows us to exclude frequency non-degenerate photons created by single-pump SFWM. EDFA: erbium-doped fibre amplifier; PC: polarization controller.

in continuous-variable quantum computation and Gaussian boson sampling[1,2,10].

Our system consists of a 2D chequerboard lattice of ring resonators (Fig. 1a)[35,36]. The rings (blue) at the lattice sites are coupled to their nearest and next-nearest neighbours using another set of rings, which we call the link rings[18,20]. The gap between the link and the site rings sets the strength J of the evanescent field coupling between the site rings and is the same for both the nearest and next-nearest neighbour site rings. The resonance frequencies of the link rings are detuned from those of the site rings such that the link rings act as waveguides connecting site rings. More importantly, depending on their position, the link rings introduce a direction-dependent hopping phase between the site rings. In our system, the link rings are positioned such that the hopping phases between next-nearest-neighbour site rings is always zero, and that between nearest-neighbour site rings is $\pm\pi/4$. This configuration effectively leads to the realization of a staggered synthetic magnetic field for photons such that the average magnetic flux through a unit cell of two plaquettes of the lattice is zero (shaded light green in the inset of Fig. 1a), but the flux through a single plaquette is non-zero. This coupled ring resonator configuration simulates the anomalous quantum Hall model for photons[35,36], with a Haldane-like tight-binding Hamiltonian

$$H = \sum_m \omega_0 a_m^\dagger a_m - J\left(\sum_{\langle m,n\rangle} a_n^\dagger a_m e^{-i\phi_{m,n}} + \sum_{\langle\langle m,n\rangle\rangle} a_n^\dagger a_m + \text{h.c.}\right) \quad (1)$$

Here $a_m^\dagger\,(a_m)$ is the photon creation (annihilation) operator at a lattice site m and h. c. indicates Hermitian conjugate. The summations $\langle m,n\rangle$ and $\langle\langle m,n\rangle\rangle$ are over the nearest-neighbour and the next-nearest-neighbour lattice sites, respectively. J is the coupling strength between the lattice sites, and is the same for both nearest and next-nearest neighbours. The hopping phase $\phi_{m,n}=\pm\pi/4$ for nearest-neighbour couplings, and $\phi_{m,n}=0$ for next-nearest-neighbour couplings. The energy–momentum band structure of the lattice shows two bulk bands separated by a bandgap. For a finite lattice, the bandgap hosts topological edge states that are confined to the boundary of the lattice. More importantly, the edge states exhibit a linear dispersion, and are robust against disorders such as a mismatch in the ring resonance frequencies[22,35,36]. The band structure and the presence of edge states in the lattice can be probed by measuring the transmission and the delay spectra of the lattice from input to the output port. The simulated transmission and delay spectra for an 8×8 lattice of site rings are shown in Fig. 1b, c. The linear dispersion of the edge states manifests in the Wigner delay spectrum as a flat profile (Fig. 1c) in the range $\delta\omega=[-1,1]J$, where $\delta\omega=\omega-\omega_0$ is the detuning of the excitation laser frequency ω from the ring resonance frequency ω_0, for a given longitudinal mode. In contrast, the Wigner delay in the bulk band varies substantially because, in a finite lattice, the bulk bands do not have a well defined momentum. Our system also supports a pseudo-spin degree of freedom because of the two circulation directions (clockwise and counter-clockwise) in the ring resonators. The two pseudo-spins (up and down) are time-reversed partners, and therefore experience opposite hopping phases and exhibit counter-propagating edge states[36].

Our topological source is designed to operate at telecommunications wavelengths (around 1,550 nm) and is fabricated using the silicon-on-insulator platform. The coupling strength J between the

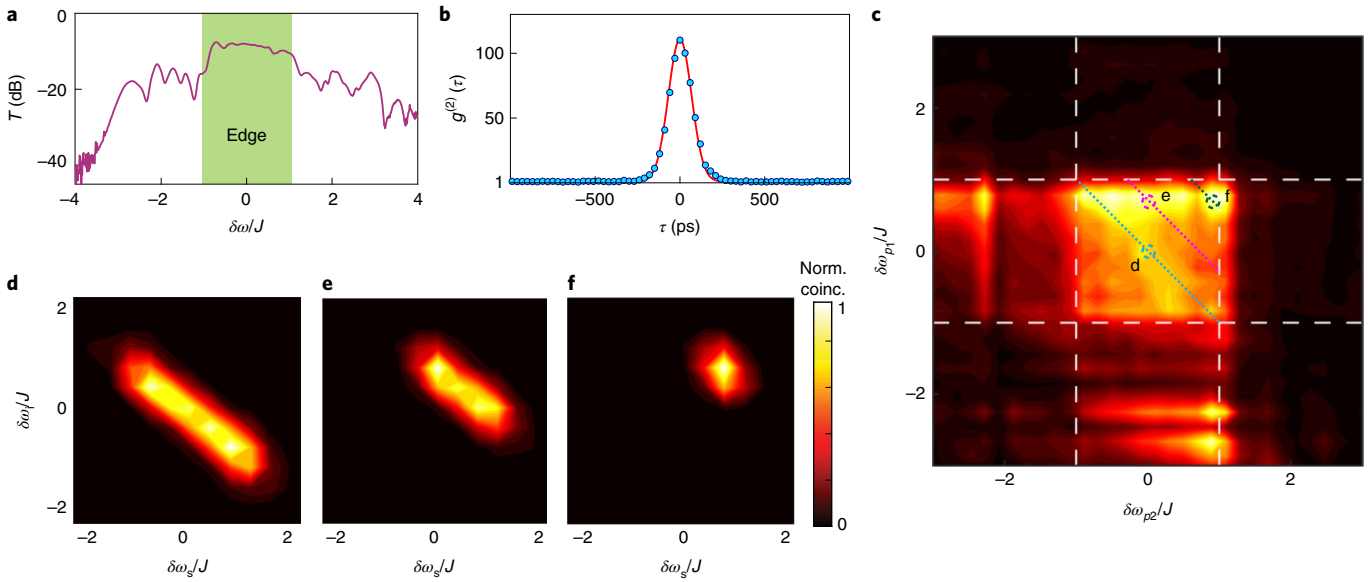

Fig. 2 | Tunability of the two-photon JSI. a, Measured transmission (T) spectrum of an anomalous Hall device, with the edge band highlighted in green. **b**, Measured second-order temporal correlation function $g_2(\tau)$ showing that the generated signal and idler photons are strongly correlated. **c**, Measured coincidence counts as function of the input pump frequency detunings $\delta\omega_{p_1}$, $\delta\omega_{p_2}$ relative to the respective longitudinal mode resonances. **d**–**f**, Measured JSI of the signal and idler photons, for input pump frequencies $(\delta\omega_{p_1}, \delta\omega_{p_2}) = (0, 0)$, $(0.8, 0)\,J$ and $(0.8, 0.8)\,J$. The colour scale indicates the number (normalized to maximum) of generated photon pairs. The pump frequencies are also indicated in **c** using labels **d**–**f**. The dashed lines in **c** show the spectra of generated photons in the edge band allowed by energy conservation. The maximum on-chip photon pair generation rate was measured to be about 3,000 $s^{-1}\,mW^{-2}$.

rings is about $(2\pi)15.6$ GHz and the free-spectral range is about $(2\pi)1$ THz. The lattice is coupled to input and output waveguides as shown in Fig. 1a. Figure 2a shows the measured transmission spectrum of the device for spin-up excitation, with the edge band highlighted in colour. The edge states for this excitation take the shorter route from input to the output coupler, as shown in Fig. 1a.

To generate indistinguishable photon pairs in this lattice, we use the $\chi^{(3)}$ nonlinearity of silicon and implement a dual-pump SFWM process (Fig. 1). We pump the lattice using two classical, continuous-wave pump beams, at frequencies ω_{p_1} and ω_{p_2}. The dual-pump SFWM then leads to the generation of correlated photon pairs, called signal and idler, at frequencies ω_s and ω_i, respectively, such that the energy conservation relation $\omega_{p_1} + \omega_{p_2} = \omega_s + \omega_i$ is satisfied. This nonlinear process is described by the Hamiltonian

$$H_{\text{nonlinear}} = \eta \sum_m (a^\dagger_{m,s}\, a^\dagger_{m,i}\, a_{m,p_1}\, a_{m,p_2} + a^\dagger_{m,p_1}\, a^\dagger_{m,p_2}\, a_{m,s}\, a_{m,i}). \quad (2)$$

Here η is the efficiency of the SFWM process, and $a^\dagger_{m,\mu}$, with $\mu = s, i, p_1, p_2$, is the photon creation operator for signal, idler or pump photons at a lattice site m.

The two-photon state generated at the output of our device is described, in general, as

$$|\Psi\rangle = \int d\omega_s d\omega_i \phi(\omega_s, \omega_i)\, \delta(\omega_s + \omega_i - \omega_{p_1} - \omega_{p_2})\, a^\dagger_s(\omega_s)\, a^\dagger_i(\omega_i)\, |\text{vac}\rangle, \quad (3)$$

where $a^\dagger_{s,i}$ are the creation operators for the signal or idler photons, $|\text{vac}\rangle$ is the vacuum state, and $\phi(\omega_s, \omega_i)$ is the two-photon spectral wavefunction. Given the fact that our ring resonator waveguides support a single transverse-electric polarized mode and the generated photons are collected from a single spatial mode (the same output port), the signal and idler photons are indistinguishable in all degrees of freedom when the two-photon spectral wavefunction is symmetric with respect to exchange of photons, that is, $\phi(\omega_s, \omega_i) = \phi(\omega_i, \omega_s)$[39,40]. Furthermore, the signal and idler photons are entangled when $\phi(\omega_s, \omega_i) \neq \phi_s(\omega_s)\,\phi_i(\omega_i)$, that is, when the two-photon spectral wavefunction cannot be expressed as a product of individual wavefunctions of signal and idler photons[40].

In our experiment, we position the two pump frequencies in two different longitudinal modes of the lattice separated by two free-spectral ranges (Ω, see Fig. 1d). The indistinguishable photon pairs are then generated in the longitudinal mode located midway between the two pump modes, that is, $\omega_{0p_1} + \omega_{0p_2} = \omega_{0s} + \omega_{0i}$ and $\omega_{0s} = \omega_{0i}$. Here $\omega_{0\mu}$, with $\mu = p_1$, p_2, s or i, is the resonance frequency of the respective longitudinal mode. We note that each of the two pump beams also generates distinguishable photon pairs via non-degenerate (single-pump) SFWM. However, because of energy conservation, these photon pairs are generated in longitudinal modes located symmetrically around the respective pump beams (Fig. 1d). Therefore, we use spectral filtering and time-resolved coincidence measurements between detected photon pairs to exclude the noise photons generated by single-pump SFWM (Fig. 1c).

To understand the nature of spectral correlations between the two pump fields and the generated photons, we first measure the number of indistinguishable photon pairs generated via dual-pump SFWM as a function of the two pump frequency detunings ($\delta\omega_{p_{1,2}} = \omega_{p_{1,2}} - \omega_{0p_{1,2}}$), relative to their respective longitudinal mode centre frequencies. As mentioned earlier, we use time-resolved correlation measurements $(g^{(2)}(\tau))$ to post-select the photon pairs generated by dual-pump SFWM. Figure 2b shows the typical temporal correlation function with pump powers $P_1 = 1$ mW and $P_2 = 3$ mW at the input of the lattice. We measure a maximum $g^{(2)}(0) \simeq 117$, which shows that the two photons are indeed correlated. We integrate over the correlation peak to get the total number of coincidence counts in a given acquisition time (here 10 s). Figure 2c shows the measured number of coincidence counts (normalized) as a function of the frequency detunings $\delta\omega_{p_1}$, $\delta\omega_{p_2}$.

Notably, we observe that the photon generation rate is maximum when both the pump frequencies are in the edge band, that is, when $\delta\omega_{p_1}, \delta\omega_{p_2} = [-1, 1]J$ (Fig. 2a). Furthermore, compared to the bulk band regions, the generation rate is relatively uniform throughout the edge band. We note that for a given choice of the two pump frequencies, energy and momentum conservation lead to spectral correlations between generated photons. However, our measurement of the number of generated photon pairs as a function of the pump frequencies does not resolve these spectral correlations.

To reveal the spectral correlations between generated signal and idler photons, we fix the input pump frequencies to be in the middle of the edge band, at $\delta\omega_{p_1} \simeq 0 \simeq \delta\omega_{p_2}$, and measure the joint-spectral intensity (JSI), $|\phi(\delta\omega_s, \delta\omega_i)|^2$ (Fig. 2d). This is the joint probability of detecting a signal photon at frequency $\delta\omega_s$ and an idler photon at frequency $\delta\omega_i$. Here $\delta\omega_{s,i}$ are the frequency detunings of the signal and idler photons relative to their respective longitudinal mode resonances. The measured correlations show that, with the two pump fields in the edge band, the spectrum of generated signal and idler photons is also limited to the edge band. This is because of the linear dispersion of the edge states that leads to efficient phase matching (momentum conservation) when all four fields are in the edge band and the confinement of the edge states to the lattice boundary, which leads to a good spatial overlap between the fields. Furthermore, both the signal and idler spectra are centred around $\delta\omega_s \simeq 0 \simeq \delta\omega_i$, which shows that they are degenerate in frequency, that is, $|\phi(\omega_s, \omega_i)|^2 = |\phi(\omega_i, \omega_s)|^2$. The JSI also shows that the signal and idler photons generated by our source are entangled, that is, $\phi(\omega_s, \omega_i) \neq \phi_s(\omega_s)\,\phi_i(\omega_i)$. We note that we use continuous-wave pumps in our experiments and the apparent width of spectral correlations along the diagonal is because of the finite spectral resolution (≈ 10 GHz $\simeq 0.64J$) of our measurements.

The energy conservation and the linear dispersion of the edge states allows us to tune the spectral bandwidth of generated photons by tuning the input pump frequencies within the edge band region. This is because of the efficient momentum conservation in the edge band that limits the spectra of generated photons also to the edge band region. To show such tunability of the spectra of generated photons, we measure the signal–idler spectral correlations for different pump frequencies in the edge band (Fig. 2e,f). When both the pump frequencies are near the side of the edge band ($\simeq 0.8J$), in Fig. 2f, we observe that the spectra of generated photons are substantially narrower (by about 4 times) than when both the pumps are in the centre of the edge band (Fig. 2d). Also, the spectra are centred around $0.8J$, which shows that the two photons are degenerate in frequency, as expected. Similarly, when the two pump frequencies are at different locations in the edge band ($\delta\omega_{p_1} \simeq 0.8J, \delta\omega_{p_2} \simeq 0$), we observe that the spectra of generated photons are centred around $0.4J$, with a bandwidth larger than that with both the pumps in the side of the edge band (Fig. 2e).

Though our JSI measurements show that the signal and idler photons are degenerate in frequency, $|\phi(\omega_s, \omega_i)|^2 = |\phi(\omega_i, \omega_s)|^2$, these measurements do not confirm their indistinguishability, which requires phase-coherence such that $\phi(\omega_s, \omega_i) = \phi(\omega_i, \omega_s)$[39,40]. A way to unambiguously confirm the indistinguishability of generated signal and idler photons is to perform HOM interference[41] between the two photons. In HOM interference, when two indistinguishable photons arrive simultaneously at the two input ports of a beamsplitter, they bunch together at the output of the beamsplitter. We emphasize that HOM interference between correlated signal and idler photons (generated by the same source) only requires the two-photon spectral wavefunction to be symmetric, $\phi(\omega_s, \omega_i) = \phi(\omega_i, \omega_s)$, but not necessarily separable, $\phi(\omega_s, \omega_i) = \phi_s(\omega_s)\,\phi_i(\omega_s)$[39,40].

In HOM interference the two photons arrive separately, one photon in each of the two input ports of the beamsplitter. However, in our topological source, both the photons are in a single spatial mode, they have the same polarization, and they are degenerate in frequency. Therefore, we cannot deterministically split the two photons into two spatial modes using a normal beamsplitter, which creates at its output a superposition of states where either one photon is in each port, or two photons are in the same port (see Supplementary section 3, and refs. [4,37]). Nevertheless, when the input to the beamsplitter is a path-entangled two-photon state of the form $|20\rangle_{A,B} + |02\rangle_{A,B}$, that is, when both the photons arrive either at the input port A or at port B of the beamsplitter, then the two-photon state at the output ports C, D of the beamsplitter is deterministic with one photon in each port, that is, $|11\rangle_{C,D}$. Here the state $|nm\rangle_{A(C),B(D)}$ refers to n photons in the input(output) port A(C) of the beamsplitter and m photons in the input(output) port B(D) (see Supplementary section 3, and refs. [4,37]). This scenario, in fact, corresponds to time-reversed HOM interference of two photons[37].

To deterministically split the two photons, so that we can later perform HOM interference between them, we use our topological source in a Sagnac interferometer (formed by beamsplitter BS-1, Fig. 3a)[4,37]. In this configuration, both the pseudo-spins (up and down) associated with our source are simultaneously pumped. Because they are time-reversed partners, the pump beams corresponding to the two pseudo-spins propagate through the same edge state, but in opposite directions, and generate a path-entangled two-photon state $|20\rangle_{A,B} + e^{-i\delta}|02\rangle_{A,B}$ at ports A, B of the beamsplitter BS-1 (Fig. 3a). We note that the strength of SFWM interaction in our experiment is very weak, such that the probability of generating two photon pairs, one in each arm of the Sagnac interferometer, is small. The relative phase δ of two-photon entangled state can be set to 0 or π by appropriately choosing the input ports for the two pump beams at the Sagnac beamsplitter (BS-1 in Fig. 3a)[4]. When both the pumps are in the same port of the BS-1 (port C or port D), the phase $\delta = \pi$, and the two photons bunch at the output of BS-1, that is, they appear together at either port C or port D of BS-1 (Fig. 3c). In contrast, when the two pumps are in different ports of the beamsplitter BS-1 (one in port C, and the other in port D), the phase $\delta = 0$ and it leads to anti-bunching of photons such that the photons are deterministically separated at the output of the BS-1 (Fig. 3b). We use two circulators to collect the photons at ports C and D. For $\delta = 0$, we measure the total probability of bunching (in either port C or port D), $g^{(2)}(0) = 0.05(1)$, which shows that the two photons are predominantly in the state $|11\rangle_{C,D}$. For $\delta = \pi$, we measure $g^{(2)}(0) = 0.93(1)$, which shows that the two photons are still in the same spatial mode (port C or port D). We emphasize that the use of a Sagnac interferometer, with the two pump beams injected at different input ports, alleviates the need for any active stabilization of our source.

To demonstrate HOM interference we set $\delta = 0$ such that the two photons are deterministically separated in the ports C and D of the beamsplitter BS-1. We pump our source in the middle of the edge band, that is, $\delta\omega_{p_1} \simeq 0 \simeq \delta\omega_{p_2}$. We introduce a relative delay τ_d between the two photons, interfere them on another beamsplitter (BS-2), and measure the coincidence counts at the output of BS-2 as we vary the delay τ_d (Fig. 3a). We see a HOM dip in the coincidence counts, with a visibility of 88(10)%, which confirms that the two photons are indeed indistinguishable (Fig. 3d). The visibility of the HOM interference observed using the topological source compares well with that observed using single waveguides and ring resonators[3,4].

We note that the temporal width of the HOM interference dip is inversely related to the spectral width of the JSI (along the line $\delta\omega_s = -\delta\omega_i$), which characterizes the two-photon state. As we demonstrated in Fig. 2d–f, we can control the JSI of generated photons in our source by simply tuning the input pump frequencies (Fig. 2). To demonstrate similar control in the HOM interference, we set the two pump frequencies to be at one of the extremes of the edge band $\delta\omega_{p_1} \simeq 0.8J \simeq \delta\omega_{p_2}$ such that the spectral width of the JSI is small (Fig. 2f). We now observe, in Fig. 3e, that the temporal width

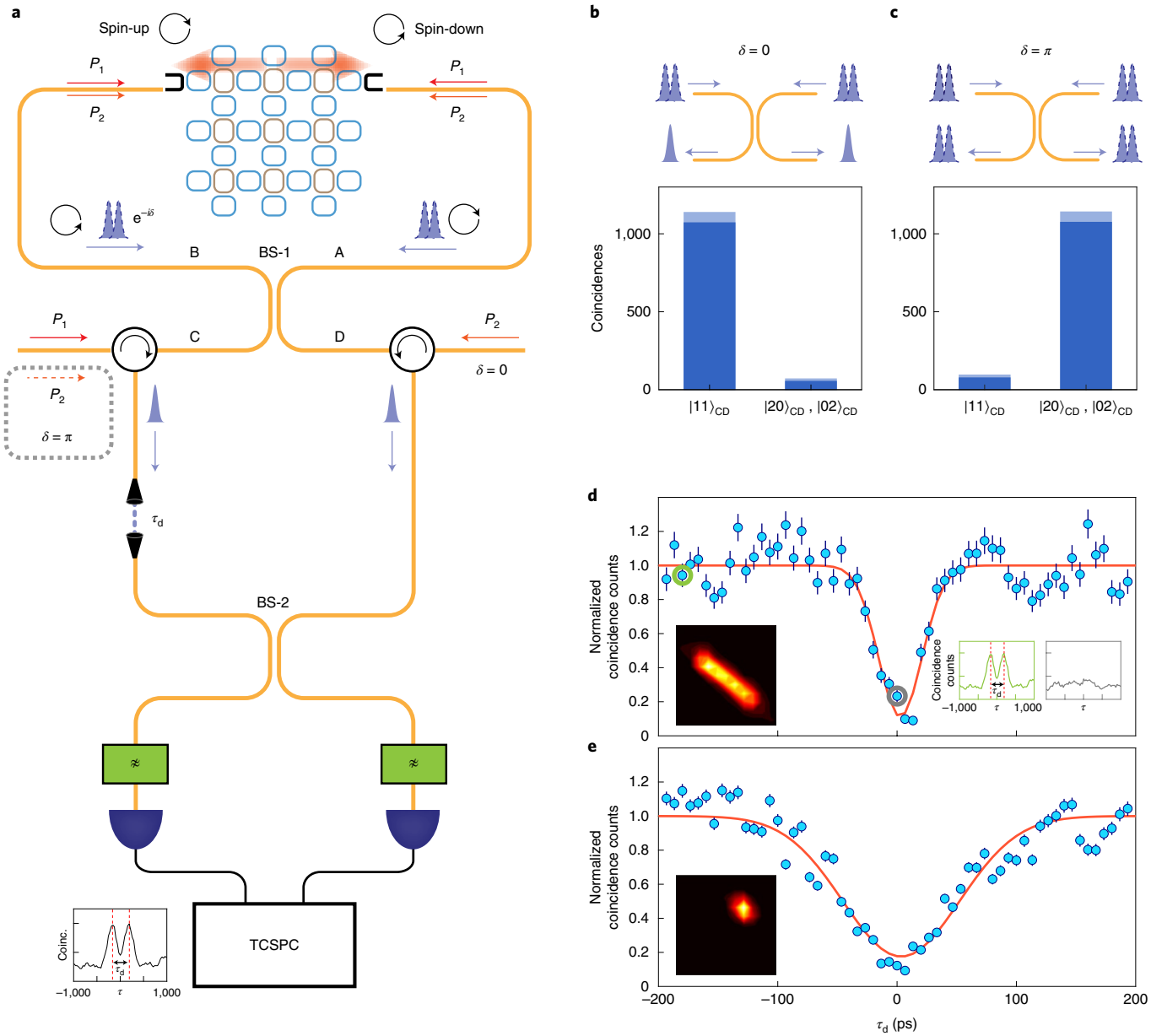

Fig. 3 | Indistinguishability of the generated photons. a, Schematic of the Sagnac interferometer setup used to deterministically split the two photons via time-reversed HOM interference of a path-entangled two-photon state (at beamsplitter BS-1), and subsequently, realize HOM interference at beamsplitter BS-2 with a variable delay τ_d between the two photons. **b**,**c**, Measured two-fold coincidences at the output ports C, D of the beamsplitter BS-1, for two different configurations of the input pump beams. The photons anti-bunch ($\delta=0$) when the two pumps are in separate input ports of BS-1, and the photons bunch ($\delta=\pi$) when the pumps are in the same input port. The bar plots were obtained by integrating the time-resolved coincidence counts over a window of 600 ps (see Supplementary section 3). **d**,**e**, Measured HOM interference dip with $\delta=0$, and pump frequencies $(\delta\omega_{p_1}, \delta\omega_{p_2}) = (0, 0)$ *J*, and (0.8, 0.8) *J*, respectively. Insets show measured JSI and time-resolved coincidences between the two photons. The error bars in **b**,**c** (shaded light blue) and **d**,**e** are calculated assuming Poissonian statistics for photon counts.

of the HOM interference dip is indeed much larger (by a factor of 2.7 ± 0.4) compared to the case with both the pumps in the centre of the edge band. The discrepancy between this factor and the decrease in the spectral width (by a factor of ~4) can be accounted for by the limited spectral resolution of our JSI measurement.

Finally, we show that the two-photon state generated by our source is energy–time entangled. We use a fibre beamsplitter (Fig. 4a, Supplementary section 4) to split the two photons at the output of our source, and inject them into two Franson interferometers[38]. The path length delay in the interferometer is about 800 ps, which is much longer than $\Delta T \approx 200$ ps, the width of the second-order temporal correlation function $g^{(2)}(\tau)$ of the generated photons (see Fig. 2b). As we discussed earlier (also see Supplementary section 4), the fibre beamsplitter creates a superposition of states, with one photon in each output port or two photons in either of the output ports. However, our coincidence measurements at the outputs of the two interferometers post-select only the state where there is one photon in each output port of the beamsplitter. Furthermore, coincidence measurements that resolve the time delay in the arrival of two photons yield three peaks. The two side peaks correspond to the two cases ($|sl\rangle$, $|ls\rangle$) when one of the photons took the shorter path (s) in the interferometer, while the other took the longer path

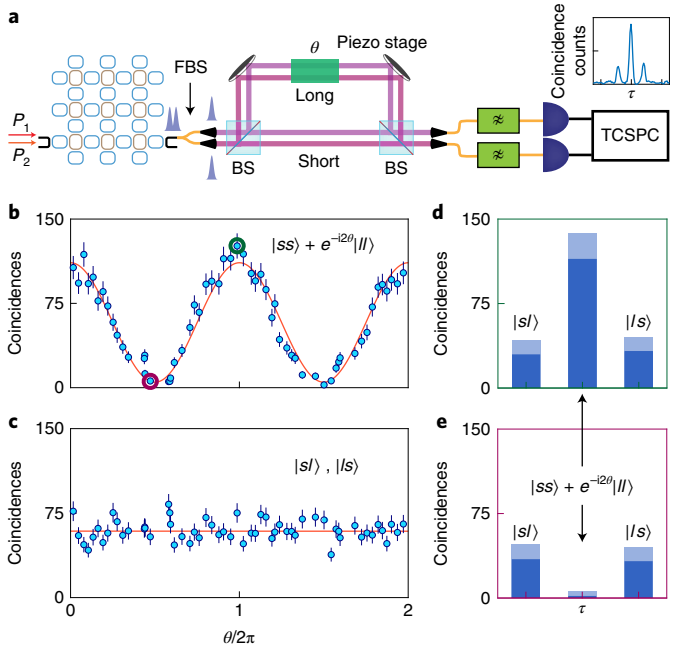

Fig. 4 | Energy–time entanglement between generated photons. a, Schematic of the Franson interferometer setup to show the energy–time entanglement of generated photon pairs. The delay between the short and the long paths is about 800 ps, much longer than the temporal correlation between the two photons. FBS: fibre beamsplitter. **b**, Measured two-fold coincidences in the central peak, that is, when both the photons travel through the same path (short or long), as a function of the interferometer phase θ. **c**, Measured two-fold coincidences in the side peaks, that is, when the photons travel through different paths and are therefore distinguishable. **d**,**e**, Measured histograms at two points indicated in **b**, showing the maximum and the minimum coincidence counts in the central peak. The counts in the side peaks are almost constant. These histograms were obtained by integrating the corresponding peaks (inset of **a**) over a window of 280 ps. The error bars in **b**,**c** and **d**,**e** (shaded light blue) are calculated assuming Poissonian statistics for photon counts. For this measurement the input pump frequencies were set to $\delta\omega_{p_1} \simeq 0.8J \simeq \delta\omega_{p_2}$.

(l, Fig. 4a). The center peak corresponds to the two cases ($|ss\rangle$, $|ll\rangle$) when both the photons took either the shorter path or the longer path, and therefore they arrive together at the two detectors with zero time delay. When we vary the phase θ of the interferometer, we observe interference fringes in the total number of coincidence counts in the centre peak, with a visibility of about 92% (Fig. 4b). This is because the two cases, $|ss\rangle$ and $|ll\rangle$, are indistinguishable at the two detectors. Furthermore, the period of interference fringes is π because the two photons acquire a total phase 2θ in the interferometer, and the corresponding state at the output of the interferometer is $\left(|ss\rangle + e^{-i2\theta}\,|ll\rangle\right)$ (Supplementary section 4). In contrast, the other two cases, where one photon travels through the shorter path and the other through the longer path ($|sl\rangle$, $|ls\rangle$), are distinguishable and accordingly yield no interference (Fig. 4c). More importantly, note that we observe interference fringes even when the path-length delay in the interferometer (about 800 ps) is much longer than the correlation time ΔT (about 200 ps, Fig. 3d) between the two photons. This demonstrates that the coherence time of the generated two-photon state ($1/\Delta\omega$), where $\Delta\omega = \Delta\omega_s + \Delta\omega_i$ is the total uncertainty in the frequency of signal and idler photons, is much longer than ΔT, such that $\Delta\omega\Delta T < 1$. Therefore, the two-photon state generated by our topological source is indeed energy–time entangled[38]. We emphasize that, similar to single-ring devices, this energy–time entanglement between generated photon pairs is because of the use of narrow-band continuous-wave pumps. By using pulsed pumps with broad-band spectra, it is indeed possible to generate indistinguishable photons pairs that are also nearly separable (see refs. [42,43] and Supplementary section 7), and can therefore be used to realize multi-photon interference schemes.

Because the edge states are topologically protected, we expect that the spectral correlations between generated photon pairs will also be robust against fabrication disorders when the two pump frequencies—and therefore the signal and idler frequencies—are in the edge band. Indeed, in ref. [32], we demonstrated the topological robustness of spectral correlations using a single-pump SFWM process[32]. To show that this topological robustness holds for dual-pump SFWM process as well, we provide numerical simulation results in Supplementary section 5. We fix the input pump frequencies to be in the centre of the edge band and calculate the spectra of generated photons for random realizations of disorder. We compare these results against those for a one-dimensional array of ring resonators, which is topologically trivial, and therefore not robust against disorder. As expected, we observe that our topological source of indistinguishable photon pairs achieves much higher spectral similarity across devices when compared to topologically trivial sources.

In summary, we have demonstrated a topological source of indistinguishable photon pairs with tunable spectral–temporal correlations. Our demonstration could lead to on-chip generation of novel quantum states of light where topological phenomena are used for robust manipulations of the photonic mode structure and quantum correlations between photons. In particular, in the low-loss regime that can be easily accessed using the commercial silicon-nitride platform, our topological devices can achieve pair-generation rates that are an order of magnitude higher than that in single-ring sources (see Supplementary section 9). Low-loss topological devices would also allow the generation of spectrally engineered or spectrally multiplexed squeezed light[5–7,44] for applications in continuous-variable photonic quantum computation. On a more fundamental level, nonlinear parametric processes such as four-wave mixing are inherently non-Hermitian in nature, that is, they do not conserve particle number. Therefore, our system paves the way for investigations of the rich interplay between topology, nonlinear and non-Hermitian physics, and quantum photonics processes to realize novel topological phases that are unique to photons.

Online content

Any methods, additional references, Nature Research reporting summaries, source data, extended data, supplementary information, acknowledgements, peer review information; details of author contributions and competing interests; and statements of data and code availability are available at https://doi.org/10.1038/s41566-021-00810-1.

Received: 18 May 2020; Accepted: 31 March 2021;

References

1. Braunstein, S. L. & van Loock, P. Quantum information with continuous variables. *Rev. Mod. Phys.* **77**, 513–577 (2005).
2. Hamilton, C. S. et al. Gaussian boson sampling. *Phys. Rev. Lett.* **119**, 170501 (2017).
3. Silverstone, J. W. et al. On-chip quantum interference between silicon photon-pair sources. *Nat. Photon.* **8**, 104 (2014).
4. He, J. et al. Ultracompact quantum splitter of degenerate photon pairs. *Optica* **2**, 779–782 (2015).
5. Vernon, Z. et al. Scalable squeezed-light source for continuous-variable quantum sampling. *Phys. Rev. Appl.* **12**, 064024 (2019).
6. Zhao, Y. et al. Near-degenerate quadrature-squeezed vacuum generation on a silicon-nitride chip. *Phys. Rev. Lett.* **124**, 193601 (2020).
7. Zhang, Y. et al. Squeezed light from a nanophotonic molecule. *Nat. Commun.* **12**, 2233 (2021).

8. Dutt, A. et al. On-chip optical squeezing. *Phys. Rev. Appl.* **3**, 044005 (2015).
9. Vaidya, V. D. et al. Broadband quadrature-squeezed vacuum and nonclassical photon number correlations from a nanophotonic device. *Sci. Adv.* **6**, eaba9186 (2020).
10. Pfister, O. Continuous-variable quantum computing in the quantum optical frequency comb. *J. Phys. B* **53**, 012001 (2019).
11. Asavanant, W. et al. Generation of time-domain-multiplexed two-dimensional cluster state. *Science* **366**, 373–376 (2019).
12. Larsen, M. V., Guo, X., Breum, C. R., Neergaard-Nielsen, J. S. & Andersen, U. L. Deterministic generation of a two-dimensional cluster state. *Science* **366**, 369–372 (2019).
13. Haldane, F. D. M. & Raghu, S. Possible realization of directional optical waveguides in photonic crystals with broken time-reversal symmetry. *Phys. Rev. Lett.* **100**, 013904 (2008).
14. Lu, L., Joannopoulos, J. D. & Soljačić, M. Topological photonics. *Nat. Photon.* **8**, 821 (2014).
15. Khanikaev, A. B. & Shvets, G. Two-dimensional topological photonics. *Nat. Photon.* **11**, 763–773 (2017).
16. Ozawa, T. et al. Topological photonics. *Rev. Mod. Phys.* **91**, 015006 (2019).
17. Wang, Z., Chong, Y., Joannopoulos, J. D. & Soljačić, M. Observation of unidirectional backscattering-immune topological electromagnetic states. *Nature* **461**, 772–775 (2009).
18. Hafezi, M., Demler, E. A., Lukin, M. D. & Taylor, J. M. Robust optical delay lines with topological protection. *Nat. Phys.* **7**, 907 (2011).
19. Kraus, Y., Lahini, Y., Ringel, Z., Verbin, M. & Zilberberg, O. Topological states and adiabatic pumping in quasicrystals. *Phys. Rev. Lett.* **109**, 106402 (2012).
20. Hafezi, M., Mittal, S., Fan, J., Migdall, A. & Taylor, J. Imaging topological edge states in silicon photonics. *Nat. Photon.* **7**, 1001 (2013).
21. Rechtsman, M. C. et al. Photonic Floquet topological insulators. *Nature* **496**, 196–200 (2013).
22. Mittal, S. et al. Topologically robust transport of photons in a synthetic gauge field. *Phys. Rev. Lett.* **113**, 087403 (2014).
23. St-Jean, P. et al. Lasing in topological edge states of a one-dimensional lattice. *Nat. Photon.* **11**, 651–656 (2017).
24. Bahari, B. et al. Nonreciprocal lasing in topological cavities of arbitrary geometries. *Science* **358**, 636–640 (2017).
25. Bandres, M. A. et al. Topological insulator laser: experiments. *Science* **359**, eaar4005 (2018).
26. Lu, L., Gao, H. & Wang, Z. Topological one-way fiber of second Chern number. *Nat. Commun.* **9**, 5384 (2018).
27. Cheng, X. et al. Robust reconfigurable electromagnetic pathways within a photonic topological insulator. *Nat. Mater.* **15**, 542–548 (2016).
28. Zhao, H. et al. Non-Hermitian topological light steering. *Science* **365**, 1163–1166 (2019).
29. Barik, S. et al. A topological quantum optics interface. *Science* **359**, 666–668 (2018).
30. Tambasco, J.-L. et al. Quantum interference of topological states of light. *Sci. Adv.* **4**, eaat3187 (2018).
31. Wang, Y. et al. Topological protection of two-photon quantum correlation on a photonic chip. *Optica* **6**, 955–960 (2019).
32. Mittal, S., Goldschmidt, E. A. & Hafezi, M. A topological source of quantum light. *Nature* **561**, 502 (2018).
33. Blanco-Redondo, A., Bell, B., Oren, D., Eggleton, B. J. & Segev, M. Topological protection of biphoton states. *Science* **362**, 568–571 (2018).
34. Haldane, F. D. M. Model for a quantum Hall effect without Landau levels: condensed-matter realization of the 'parity anomaly'. *Phys. Rev. Lett.* **61**, 2015 (1988).
35. Leykam, D., Mittal, S., Hafezi, M. & Chong, Y. D. Reconfigurable topological phases in next-nearest-neighbor coupled resonator lattices. *Phys. Rev. Lett.* **121**, 023901 (2018).
36. Mittal, S., Orre, V. V., Leykam, D., Chong, Y. D. & Hafezi, M. Photonic anomalous quantum Hall effect. *Phys. Rev. Lett.* **123**, 043201 (2019).
37. Chen, J., Lee, K. F. & Kumar, P. Deterministic quantum splitter based on time-reversed Hong-Ou-Mandel interference. *Phys. Rev. A* **76**, 031804 (2007).
38. Franson, J. D. Bell inequality for position and time. *Phys. Rev. Lett.* **62**, 2205–2208 (1989).
39. Branning, D., Grice, W., Erdmann, R. & Walmsley, I. A. Interferometric technique for engineering indistinguishability and entanglement of photon pairs. *Phys. Rev. A* **62**, 013814 (2000).
40. Harder, G. An optimized photon pair source for quantum circuits. *Opt. Expr.* **21**, 13975–13985 (2013).
41. Hong, C. K., Ou, Z. Y. & Mandel, L. Measurement of subpicosecond time intervals between two photons by interference. *Phys. Rev. Lett.* **59**, 2044 (1987).
42. Helt, L. G., Yang, Z., Liscidini, M. & Sipe, J. E. Spontaneous four-wave mixing in microring resonators. *Opt. Lett.* **35**, 3006–3008 (2010).
43. Vernon, Z. et al. Truly unentangled photon pairs without spectral filtering. *Opt. Lett.* **42**, 3638–3641 (2017).
44. Peano, V., Houde, M., Marquardt, F. & Clerk, A. A. Topological quantum fluctuations and traveling wave amplifiers. *Phys. Rev. X* **6**, 041026 (2016).

Methods

Our devices are fabricated using the complementary metal–oxide–semiconductor (CMOS) compatible silicon-on-insulator platform at a commercial foundry (IMEC Belgium). The ring waveguides are about 510 nm wide, about 220 nm high and, at telecommunications wavelengths (around 1,550 nm), they support a single transverse-electric polarized mode. The ring length is about 70 μm with a free-spectral range of around $(2\pi)1$ THz. The coupling gap between the rings is 0.180 nm, and it results in a coupling strength of $J \simeq (2\pi)15.6$ GHz. The lattice is coupled to input and output waveguides, as shown in Fig. 1. At the ends of the input/output waveguides, we use grating couplers to couple light from a standard single-mode fibre into the waveguide.

We use two tunable lasers (Santec TSL 710) to pump the lattice. The two pump lasers are amplified using using two erbium-doped fibre amplifiers (Amonics), and two tunable filters (OzOptics) are used to reduce the noise photons generated by the erbium-doped fibre amplifiers. The pump lasers are combined using a 50:50 fibre beamsplitter, and coupled to the input port of the lattice using a grating coupler. The photons generated at the output port of the lattice are collected into a single-mode fibre using another grating coupler. We use cascaded wavelength-division multiplexing (WDM) filters to filter out the pump photons, and use two superconducting nanowire detectors (PhotonSpot) and a time-correlated single photon counter (HydraHarp) to perform time-resolved coincidence detection of photons. For the JSI measurements (reported in Fig. 2) we use two narrow-band tunable filters (Exfo XTM-50) before the nanowire detectors. For demonstration of energy-time entanglement we used a single Michelson interferometer (see Supplementary Information for details).

Data availability

The data that support the findings of this study are available on reasonable request. Correspondence should be addressed to S.M. (mittals@umd.edu).

Acknowledgements

This research was supported by the Air Force Office of Scientific Research AFOSR-MURI grant FA9550-16-1-0323, Office of Naval Research ONR-MURI grant N00014-20-1-2325, Army Research Laboratory grant W911NF1920181, and NSF grant PHY1820938. We thank Q. Quraishi for providing the nanowire detectors.

Author contributions

S.M. and V.V.O. contributed equally. S.M. conceived and designed the experiment, and performed numerical simulations. V.V.O. and S.M. performed the measurements. E.A.G. contributed to source characterization. M.H. supervised the project. All authors contributed to analysing the data and writing the manuscript.

Competing interests

A US provisional patent application (no. 63/028,468) has been filed based on the results reported in this manuscript.

Additional information

Supplementary information The online version contains supplementary material available at https://doi.org/10.1038/s41566-021-00810-1.

Correspondence and requests for materials should be addressed to S.M.

Peer review information *Nature Photonics* thanks the anonymous reviewers for their contribution to the peer review of this work.

Reprints and permissions information is available at www.nature.com/reprints.

Supplementary Information: Tunable quantum interference using a topological source of indistinguishable photon pairs

Sunil Mittal[1, 2, *, †], Venkata Vikram Orre[1, 2, *], Elizabeth A. Goldschmidt[3], and Mohammad Hafezi[1, 2, 4]
[1]*Joint Quantum Institute, NIST/University of Maryland, College Park, Maryland 20742, USA*
[2]*Department of Electrical and Computer Engineering and IREAP, University of Maryland, College Park, Maryland 20742, USA*
[3]*Department of Physics, University of Illinois at Urbana-Champaign, Urbana, Illinois 61801, USA*
[4]*Department of Physics, University of Maryland, College Park, MD 20742, USA*
[*]*S.M. and V.V.O. contributed equally and*
[†]*Email: mittals@umd.edu*

S1: COINCIDENCES AND CAR AS A FUNCTION OF PUMP POWER

The number of coincidence counts generated in the dual-pump spontaneous four-wave mixing (DP-FWM) process depend on the product of the input pump powers as $P_{p_1}P_{p_2}$, where P_{p_i} is the power of the pump with index $i = 1, 2$. In contrast, the number of coincidence counts generated in a single-pump spontaneous four-wave mixing (SP-FWM) process vary as $P_{p_i}^2$. To verify that the coincidence counts detected in our setup are generated by the DP-SFWM process, we fix one of the input pump powers, at 3 mW (on-chip), and measure the coincidence counts as we vary the other pump power. From Fig.S1a, we see that the number of measured coincidence counts (accumulated over 180 seconds) indeed increase linearly with one of the pump powers.

We also measure the coincidences-to-accidentals ratio (CAR) which is an indication of the signal to noise ratio of a source. To do that, we integrate the measured $g^{(2)}(\tau)$ (see Fig.2b of the main text) around the peak to calculate the actual coincidence counts, and divide it by the mean coincidence counts at $\tau \gg 0$ which are the accidental coincidences. Our source achieves a maximum CAR of ≈ 53. We also measured CAR as we vary one of the pump powers (say P_{p_2}) while the other pump power (say P_{p_1}) is fixed (at 3 mW), and the result is shown in Fig.S1b. As expected, we find that the CAR follows the relation [1]

$$CAR = \frac{\eta P_{p_1} P_{p_2}}{(P_{p_1}^2 + P_{p_2}^2 + P_{p_1}P_{p_2})^2}, \tag{S1}$$

where η is a fitting parameter. For low P_{p_2}, the CAR is limited by the noise photons generated by pump p_1 via single-pump SFWM process.

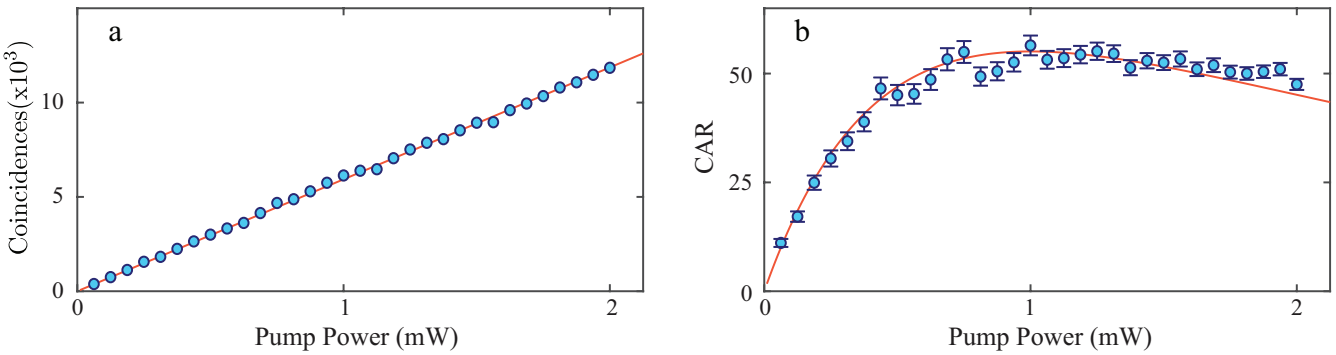

FIG. S1. **a** Coincidences, and **b** CAR as function of one of the pumps powers, while the other pump power is fixed at 3 mW.

S2: JSI IN THE BULK BAND

Figure S2 shows the measured the joint-spectral intensity (JSI) of the signal and idler photons, when the input pump frequencies are in the bulk band of the device, that is, when $(\delta\omega_{p_1}, \delta\omega_{p_2}) = (-2.42, -2.42)\, J$, and $(-1.82, -2.42)\, J$. While the JSI is still along the anti-diagonal $\delta\omega_s = -\delta\omega_i$ because of energy conservation, we observe that the JSI shows presence of distinct modes. More importantly, this mode pattern changes randomly as we tune the input pump frequencies. In contrast, when both the pump frequencies are in the edge band (Fig. 2 of the main text), the JSI is relatively uniform, and only the bandwidth of the

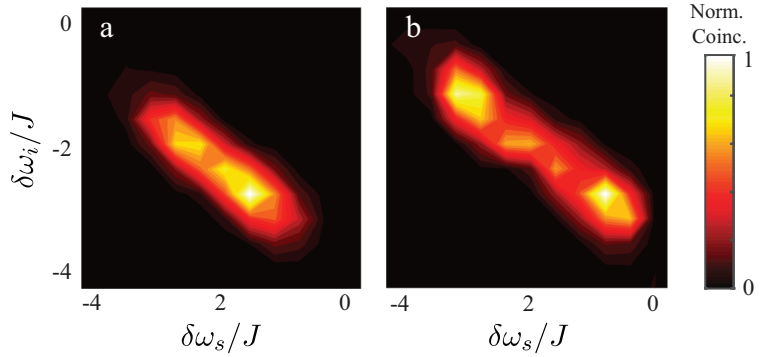

FIG. S2. Measured JSI when the input pumps frequencies are in the bulk band, **a** $(\delta\omega_{p_1}, \delta\omega_{p_2}) = (-2.42, -2.42)\, J$, **b** $(\delta\omega_{p_1}, \delta\omega_{p_2}) = (-1.82, -2.42)\, J$. The JSI shows presence of distinct modes, that change with pump frequencies.

JSI changes as we change the pump frequencies. This behavior of bulk band is because, unlike the edge band, it does not have a well-defined momentum and its dispersion is very sensitive to fabrication disorders.

S3: TIME-REVERSED HOM INTERFERENCE

As we mentioned in the main text, the signal and idler photons generated by our topological source are in a single spatial mode, with the same polarization (TE), and are degenerate in frequency. Therefore, we can not use a normal beamsplitter to deterministically split the two photons into two spatial modes. Consider a two-photon state arriving at a beamsplitter such that both the photons are at the input port A, that is,

$$|\Psi\rangle_{in} = |2,0\rangle_{A,B} = \frac{1}{\sqrt{2}}\, a_A^\dagger a_A^\dagger\, |vac\rangle\,. \tag{S2}$$

Here $a_A^\dagger$ and $a_B^\dagger$ are the photon creation operators at the input port A and B, respectively, and they can be expressed in terms of the photon operators at the output ports C and D of the beamsplitter as

$$a_A^\dagger = \frac{a_C^\dagger - i a_D^\dagger}{\sqrt{2}} \qquad a_B^\dagger = \frac{-i a_C^\dagger + a_D^\dagger}{\sqrt{2}}. \tag{S3}$$

Therefore, the two-photon state at the output of the beamsplitter is given as

$$\begin{aligned} |\Psi\rangle_{out} &= \frac{1}{2\sqrt{2}} \left(a_C^\dagger - i a_D^\dagger\right)\left(a_C^\dagger - i a_D^\dagger\right) |vac\rangle \\ &= \frac{1}{2\sqrt{2}} \left(a_C^\dagger a_C^\dagger - a_D^\dagger a_D^\dagger - i a_C^\dagger a_D^\dagger - i a_D^\dagger a_C^\dagger\right) |vac\rangle \\ &= \frac{1}{2} \left(|2,0\rangle_{C,D} - |0,2\rangle_{C,D} - i\,\sqrt{2}\,|1,1\rangle_{C,D}\right) \end{aligned} \tag{S4}$$

As evident, the output of the beamsplitter will contain one photon in each port C and D with a probability of 0.5, and two photons in port C or in port D with a probability of 0.25 each. Clearly, we can not use a normal beamsplitter to deterministically split the two photons and perform the HOM interference.

Now consider the case when the input to the beamsplitter is a path-entangled two-photon state of the form [2, 3]

$$|\Psi\rangle_{in} = \frac{1}{\sqrt{2}} \left(|2,0\rangle_{A,B} + e^{-i\delta}\,|0,2\rangle_{A,B}\right) = \frac{1}{2} \left(a_A^\dagger a_A^\dagger + e^{-i\delta} a_B^\dagger a_B^\dagger\right) |vac\rangle\,. \tag{S5}$$

In this case the two-photon state at the output of the beamsplitter is

$$\begin{aligned} |\Psi\rangle_{out} &= \frac{1}{4} \left\{\left(1 - e^{-i\delta}\right) \left(a_C^\dagger a_C^\dagger - a_D^\dagger a_D^\dagger\right) - i\left(1 + e^{-i\delta}\right) \left(a_C^\dagger a_D^\dagger + a_D^\dagger a_C^\dagger\right)\right\} |vac\rangle \\ &= \frac{1}{2\sqrt{2}} \left\{\left(1 - e^{-i\delta}\right) \left(|2,0\rangle_{C,D} - |0,2\rangle_{C,D}\right) - i\sqrt{2}\left(1 + e^{-i\delta}\right) |1,1\rangle_{C,D}\right\} \end{aligned} \tag{S6}$$

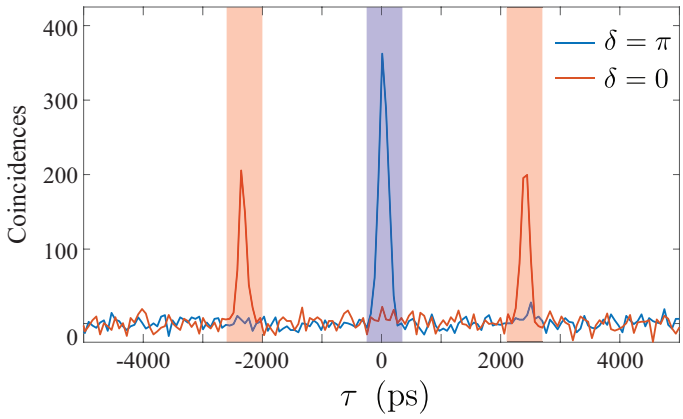

FIG. S3. Time-resolved coincidence measurement plots used to obtain bar plots in Fig.3 b,c of the main text. These plots were acquired using the setup of Fig.3a of the main text, with delay τ_d set to ≈ 2400 ps. The integration window for each peak, shown by dashed lines, was chosen to be 600 ps.

Clearly, when the phase of the path-entangled two-photon state $\delta = 0$, the state at the output of the beamsplitter is deterministic with only one photon in each arm, that is,

$$|\Psi\rangle_{out} = |1,1\rangle_{C,D}\,. \tag{S7}$$

In this case, the two-photons at the output are always anti-bunched. This situation corresponds exactly to that of a time-reversed HOM interference [2].

In contrast, when $\delta = \pi$, the two photons at the output of the beamsplitter are always bunched with

$$|\Psi\rangle_{out} = \frac{1}{2}\left(|2,0\rangle_{C,D} - |0,2\rangle_{C,D}\right), \tag{S8}$$

which is the same state as the input.

In our experiment, we set the phase δ by choosing the pump ports in the Sagnac interferometer setup (Fig. 3a of the main text). When both the pumps are injected from the same port (Port C or Port D), the beamsplitter BS-1 introduces a relative phase $\delta = \pi$ between pumps in the port A and port B. When the pumps are injected from different ports (one in Port C and one in Port D), the relative phase $\delta = 0$. This relative phase δ of the pump fields gets imprinted on the two-photon state generated in the DP-SFWM process.

To measure the anti-bunching and bunching of photons with $\delta = 0$, and $\delta = \pi$, respectively, we used the same setup as shown in Fig.3a of the main text. However, we increased the path length delay $\tau_d \approx 2400$ ps, much longer than the correlation time of the photon pairs. This ensured that there are no single-photon or two-photon interference effects. The result of time-resolved coincidence measurements at the two detectors are shown in Fig.S3 for $\delta = 0$ and $\delta = \pi$.

When the two-photon state at the output of beamsplitter BS-1 is anti-bunched, that is, of the form $|1,1\rangle_{C,D}$ (see Eq.S7), the path length difference between the two arms introduces a relative delay $\tau_d \approx 2400$ ps between the two photons as they arrive at the detectors. Therefore, in time-resolved coincidence measurements, anti-bunched photons show up as coincidence counts around $\tau \approx \pm 2400$ ps, the side-peaks in Fig.S3. In contrast, when the two-photon state at the output of beamsplitter BS-1 is bunched, of the form $|2,0\rangle_{C,D}$ or $|0,2\rangle_{C,D}$ (see Eq.S8), there is no relative delay between the two photons and they arrive together at the detectors. In this case, the coincidence counts peak near $\tau = 0$.

From Fig.S3, we see that for $\delta = 0$ the number of coincidence counts near $\tau = 0$ is negligible. This indicates that for $\delta = 0$ the photons are anti-bunched, and they are predominantly in the state $|1,1\rangle_{C,D}$. For $\delta = \pi$, the number of coincidence counts is maximum near $\tau = 0$ which shows that they are bunched, in a superposition of states $|2,0\rangle_{C,D}$ and $|0,2\rangle_{C,D}$. The bar plots shown in Fig.3b,c of the main text are obtained by integrating the coincidence counts in Fig.S3 over a window of 600 ps (as shown in the figure). Furthermore, we sum the coincidence counts in the two side-peaks because they are both contributed by the same state $|1,1\rangle_{C,D}$. The probability of bunching, $g^{(2)}(\tau = 0)$, is then calculated as the ratio of coincidence counts (integrated) in the center peak (bunched photons) to the total number of coincidence counts in the center and side peaks (anti-bunched). Note that we have corrected for accidental coincidence counts in the plots of Fig.S3. The accidental coincidences were estimated by averaging the raw coincidence counts in regions far away from the actual coincidence peaks.

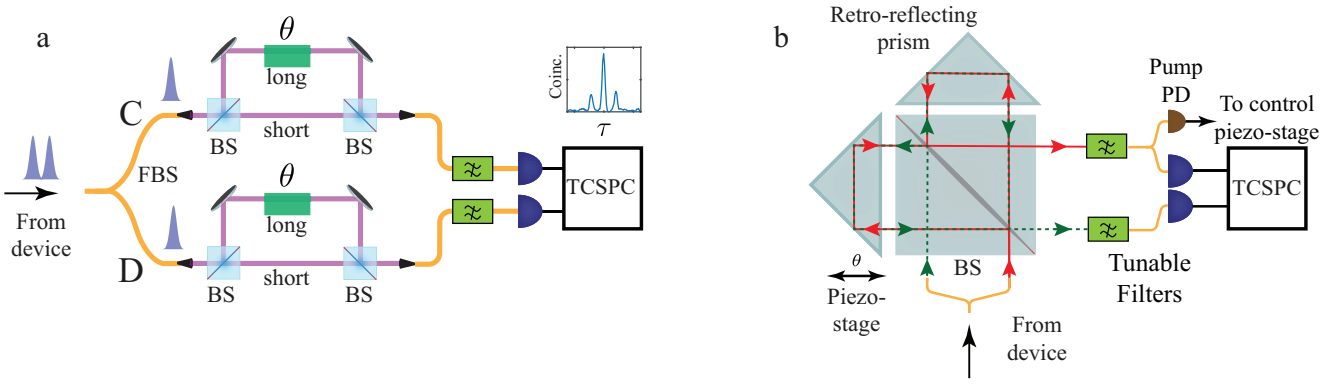

FIG. S4. **a** Simplified schematic of the Franson setup used to demonstrate energy-time entanglement between between generated photon pairs. **b** Schematic of the actual Franson interferometer setup implemented using Michelson configuration. FBS: fiber beamsplitter, BS: beamsplitter, PD: photo-detector, TCSPC: time-correlated single photon counter

S4: FRANSON INTERFEROMETER FOR DEMONSTRATING ENERGY-TIME ENTANGLEMENT

Figure S4a shows a simplified schematic of the Franson interferometer that was used to demonstrate energy-time entanglement between generated signal and idler photon pairs [4]. The two photons generated by our topological source are first injected into a fiber beamsplitter (labelled FBS in Fig.S4a). Following Eq.S4, the two-photon state at the output of the fiber beamsplitter is a superposition of states, with one photon in each output port (labelled C and D), and two photons in either of the output ports, and is given as

$$\begin{aligned} |\Psi\rangle_{out,\text{FBS}} &= \frac{1}{2}\left(|2,0\rangle_{C,D} - |0,2\rangle_{C,D} - i\sqrt{2}\,|1,1\rangle_{C,D}\right) \\ &= \frac{1}{2\sqrt{2}}\left(a_C^\dagger a_C^\dagger - a_D^\dagger a_D^\dagger - i a_C^\dagger a_D^\dagger - i a_D^\dagger a_C^\dagger\right)|vac\rangle\,. \end{aligned} \tag{S9}$$

Each unbalanced interferometer then creates a superposition of states, labelled by the "short" path (s) and the "long" path (l) such that

$$\begin{aligned} a_C^\dagger &= a_{s,C}^\dagger - e^{-i\theta} a_{l,C}^\dagger \\ a_D^\dagger &= a_{s,D}^\dagger - e^{-i\theta} a_{l,D}^\dagger \end{aligned} \tag{S10}$$

Here, $a_{s,C}^\dagger$ represents photon creation operation corresponding to "short" path (s) in the interferometer connected to port C, and so on. We have assumed that the relative phase θ of both the interferometers is the same (see below). Also, for simplicity, we have dropped the normalization factors. The two-photon state at the two outputs of the two Franson interferometers (FI) is then described as

$$\begin{aligned} |\Psi\rangle_{out,\text{FI}} = &\left\{a_{s,C}^\dagger a_{s,C}^\dagger + e^{-i2\theta} a_{l,C}^\dagger a_{l,C}^\dagger - 2e^{-i\theta} a_{s,C}^\dagger a_{l,C}^\dagger\right\} \\ - &\left\{a_{s,D}^\dagger a_{s,D}^\dagger + e^{-i2\theta} a_{l,D}^\dagger a_{l,D}^\dagger - 2e^{-i\theta} a_{s,D}^\dagger a_{l,D}^\dagger\right\} \\ - i&\left\{a_{s,C}^\dagger a_{s,D}^\dagger + e^{-i2\theta} a_{l,C}^\dagger a_{l,D}^\dagger - e^{-i\theta}\left(a_{l,C}^\dagger a_{s,D}^\dagger + a_{s,C}^\dagger a_{l,D}^\dagger\right)\right\} \end{aligned} \tag{S11}$$

In this state, the terms in the first line indicate the scenario when both the photons are in the upper interferometer corresponding to port C of the fiber beamsplitter (FBS). Similarly, terms in the second line indicate the scenario when both the photons are in the lower interferometer corresponding to port D of the fiber beamsplitter.

For our measurements, we detect coincidence events between outputs of the upper and the lower interferometer. Therefore, our coincidence measurements project the state $|\Psi\rangle_{out,\text{FI}}$ into terms on third line where there is one photon in each port C and D.

$$\begin{aligned} |\Psi\rangle_{\text{detectors}} &= a_{s,C}^\dagger a_{s,D}^\dagger + e^{-i2\theta} a_{l,C}^\dagger a_{l,D}^\dagger - e^{-i\theta}\left(a_{l,C}^\dagger a_{s,D}^\dagger + a_{s,C}^\dagger a_{l,D}^\dagger\right) \\ &= |ss\rangle + e^{-2i\theta}\,|ll\rangle - \frac{i}{\sqrt{2}}\left(|s,l\rangle + |l,s\rangle\right) \end{aligned} \tag{S12}$$

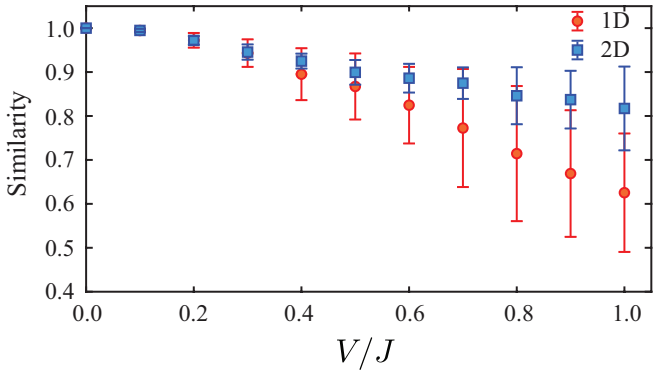

FIG. S5. Numerical simulation results comparing the similarity in the spectra of generated photons as a function of disorder for topologically trivial 1D array and 2D topological devices. As expected the spectra of generated photons in topologically trivial 1D devices are much more susceptible to disorder compared to the 2D topological devices. The simulation data was acquired for fixed input pump frequencies $(\omega_{p_1}, \omega_{p_2}) = (0, 0)J$.

The first two terms here represent the scenario when both the photons took the short path (s), or both took the long path (l) in their respective interferometers. In both these cases, the photons arrive together at the detectors, with zero time delay (the center peak in Fig.4d,e of the main text and the inset of Fig.S4a). Because we use continuous-wave pumps for our source, the detectors can not distinguish between these two possibilities, and this leads to interference fringes with phase 2θ. The last two terms represent the scenario where the photon in the C port took the long path, and photon in the D port took the short path, or vice-versa, through their respective interferometers. These two possibilities are distinguishable, and therefore, do not lead to any interference at the detectors (as shown in Fig.4c of the main text).

In our experiment, for the ease of alignment, we actually used a single Michelson interferometer to implement both the unbalanced interferometers as shown in Figure S4b. In this configuration, the relative phase θ of both the interferometers is the same. We used a piezo-controlled stage to change the phase θ. Furthermore, we used WDM filters to filter out the pump wavelength, measured the pump power using a photodetector (PD), and used this measurement to monitor the phase θ of the interferometer.

S5: ROBUSTNESS OF SPECTRAL CORRELATIONS

To numerically show the robustness of spectral correlations of our source in the presence of disorder, we perform simulations to calculate the spectra of generated photons in the presence of random disorder. We introduce the disorder using random variations in the ring resonator frequencies, where the disorder strength is given by V. We fix the input pump frequencies $(\omega_{p_1}, \omega_{p_2}) = (0, 0)J$, and average over 100 random realizations for each disorder. We then calculate the mean similarity of the disordered spectra with the spectra in the absence of any disorder. The similarity between two devices i and j is calculated by taking the mean of the inner product between two spectra and is given by,

$$S_{i,j} = \frac{\sqrt{\int \Gamma_i \Gamma_j}^2}{\int \Gamma_i \int \Gamma_j} \tag{S13}$$

where $\Gamma_{i,j}$ is the spectra of generated photons for a device i,j. We compare the results against those obtained for a topologically trivial 1D array of 10 ring resonators. As shown in Fig.S5, our topological source of indistinguishable photon pairs achieves much higher spectral similarity across devices when compared to a topologically trivial source. We also observe that the variability in the spectra of 1D devices is much higher compared to 2D devices for larger disorders. These results show the advantage of using topologically robust edge states for generating indistinguishable photon pairs [5].

S6: JSI MEASUREMENTS ON ANOTHER 2D TOPOLOGICAL DEVICE

Fig.S6 shows the transmission spectrum, number of coincidence counts as a function of the two pump frequencies, and the JSI for three different pump frequencies in the edge band, measured on another 2D topological device. This device had exactly same design parameters as the device reported in Fig.2 of the main text. However, this device was fabricated on a different chip,

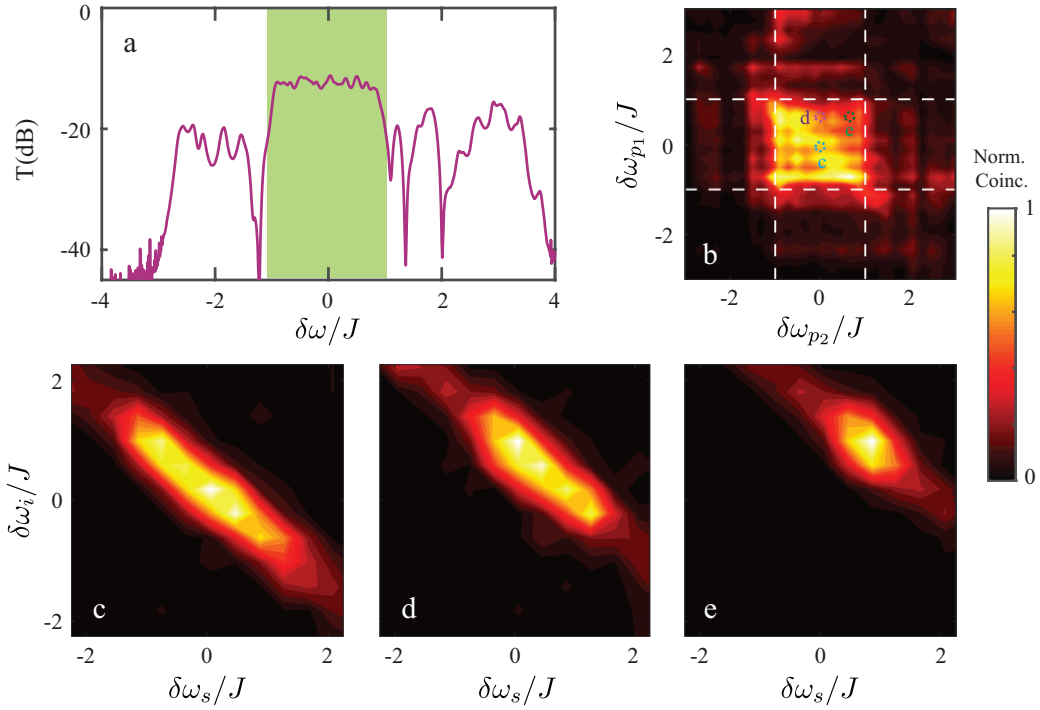

FIG. S6. **a** Measured transmission spectrum on another 2D topological device, with same design parameters as that reported in Fig. 2 of the main text, but fabricated on a different chip. **b** Number of photon pairs generated as a function of the input pump frequencies. The pair generation rate is enhanced in the edge band. **c-e** Measured JSI for three different pump positions in the edge band. Similar to Fig.2 of the main text, we can tune the spectrum of generated photons by tuning the pump frequencies.

and therefore, fabrication disorder can lead to variations in device behavior. A comparison of this device data with that reported in Fig.2 of the main text shows that although the two devices have different characteristics in the bulk bands, the behavior in the edge band is qualitatively the same. As before, we find that generation of photons pairs is enhanced when both the pump frequencies are in the edge band. Similarly, we can tune the spectra bandwidth of the two-photon wavefunction by tuning the pump frequencies within the edge band. These results once again highlight the robustness of topological edge states for generation of spectrally engineered indistinguishable photon pairs.

S7: NEARLY SEPARABLE PHOTON PAIRS USING PULSED PUMPS

In our experiment we demonstrated quantum interference between two correlated photons that are generated by the same source. As we mentioned in the main text, this interference only requires that the two photons are indistinguishable, that is, the two-photon wavefunction is symmetric under exchange of photons $\phi(\omega_s, \omega_i) = \phi(\omega_i, \omega_s)$. However, interference between photons generated by independent sources, for example, in gaussian Boson sampling or HOM interference between heralded photons, also requires the two-photon state to be separable $\phi(\omega_s, \omega_i) = \phi_s(\omega_s)\,\phi_i(\omega_s)$, that is, the two photons should not be entangled [6].

In our experiment we used continuous-wave pump lasers that naturally leads to the emergence of energy-time entanglement in the generated photon pairs. Nevertheless, by using pulsed pumps we can also generate nearly separable photon pairs, as is usually the case with all SFWM or SPDC based sources [6, 7]. In Fig.S7a,b we show the numerically simulated JSI for narrow-band pumps, and broad-band pulsed pumps, respectively. For the narrow-band pumps, we consider Gaussian pulses, each with a bandwidth (1/e) of 0.1J; and for broad-band pumps the bandwidth is 2.4J which is close to the bandwidth $(2J)$ of the edge band. For both these scenarios, both the pump pulse detunings $\delta\omega_{p_1}$ and $\delta\omega_{p_2}$ are centered around 0J. For the narrow-band pumps (Fig.S7a), the energy-time entanglement in the two photons is clearly evident because detection of an idler photon at frequency $\delta\omega_i$ deterministically projects the signal photon to a very narrow frequency band centered at $\delta\omega_s = \delta\omega_{p_1} + \delta\omega_{p_2} - \delta\omega_i$, and therefore, the two photons are not separable. For the broad-band pumps (Fig.S7b), detecting an idler photon at frequency $\delta\omega_i$ does not determine the frequency of the signal photon, and therefore, the two photons are nearly separable.

To quantify the separability of the two photons generated in each case, we calculate the reduced density matrix ρ_s for signal

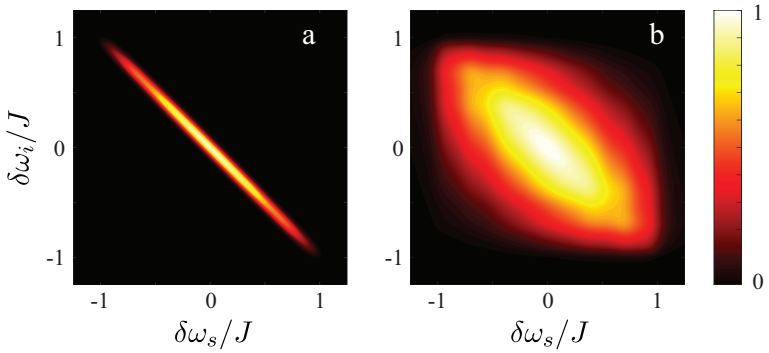

FIG. S7. Numerically simulated JSI for **a** narrow-band pump pulses with bandwidth of 0.1J, and **b** for broad-band pump pulses with bandwidth of 2.4J. The two-photon state in **b** is nearly separable.

photons following the detection of an idler photon as

$$\rho_s = \int d\omega_s d\omega_{s'}\; q_s\left(\omega_s, \omega_{s'}\right) a^\dagger\left(\omega_s\right)|0\rangle\langle 0|\, a\left(\omega_{s'}\right), \tag{S14}$$

where

$$q_s\left(\omega_s, \omega_{s'}\right) = \int d\omega_i\; \phi\left(\omega_s, \omega_i\right) \phi^*\left(\omega_{s'}, \omega_i\right). \tag{S15}$$

The separability of the two-photon state is then simply the purity (γ) of the reduced density matrix ρ_s and is calculated as

$$\gamma = Tr[\rho_s^2] = \int\int d\omega_s d\omega_{s'} \left|q\left(\omega_s, \omega_{s'}\right)\right|^2. \tag{S16}$$

For the JSI shown in Fig.S7a with narrow-band pump pulses we get a purity of $\sim 10\%$ indicating that the projected signal photon state is mixed. For the JSI of Fig.S7b with broad-band pump pulses, we get a purity of 89.6% indicating that the two-photon state is nearly separable. We note that even for a single-ring resonator SFWM based source, using Gaussian pump pulses, the maximum purity is limited to 93% [7]. Therefore, the separability of the two-photon state generated by our topological source is comparable to that generated by a single-ring resonator. Furthermore, this purity could be enhanced by spectrally shaping the pump pulses or by reducing the quality factor of the pump pulses compared to that of generated photons [7]. We could not perform such experiments because of the unavailability of tunable pulsed lasers.

S8: RESOLVING EDGE STATE RESONANCES

Because of their extended nature, the topological edge states in our devices constitute a super-ring resonator that is confined to the boundary of the lattice. The longitudinal modes of this super-ring resonator are in fact the edge state resonances. In our experiment, these individual resonances are not resolved because the coupling rate $\kappa_{ex} \approx 30$ GHz of the lattice to the input and output waveguides is much stronger than the coupling rate $J \approx 15$ GHz within the rings. By reducing κ_{ex}, for example to $0.1J$, the individual edge state resonances can be very easily resolved. Fig.S8a shows the numerically simulated transmission spectrum for such a device where the edge state resonances are clearly evident. We emphasize that this transmission spectrum repeats every FSR, that is, at every longitudinal mode resonance of the individual ring resonators.

Realizing SFWM in such a device will lead to the generation of photon pairs predominantly at the edge state resonance frequencies. For example, Fig.S8b,c show the simulated JSI of generated photon pairs, for narrow-band pump pulses (bandwidth = $0.1J$), with $(\delta\omega_{p_1}, \delta\omega_{p_2})$ centered at two edge state resonances $(0.15J, 0.15J)$ and $(0.475J, 0.475J)$, respectively. The JSI clearly shows generation of photon pairs with both the signal and idler frequencies centered around edge resonances. These JSI plots can be compared with that of Fig.S7a where the edge states resonances were not resolved. We note that the two-photon states with JSI shown in Fig.S8b,c are not separable because of the use of narrow-band pump pulses. Fig.S8d shows the JSI for the scenario where we use broad-band pump pulses, centered at $(0.15J, 0.15J)$. As expected, the two-photon state is nearly separable with the purity of the heralded photon being 86%. Such two-photon states with resolved edge resonances could be used to realize frequency-multiplexed squeezed states of light.

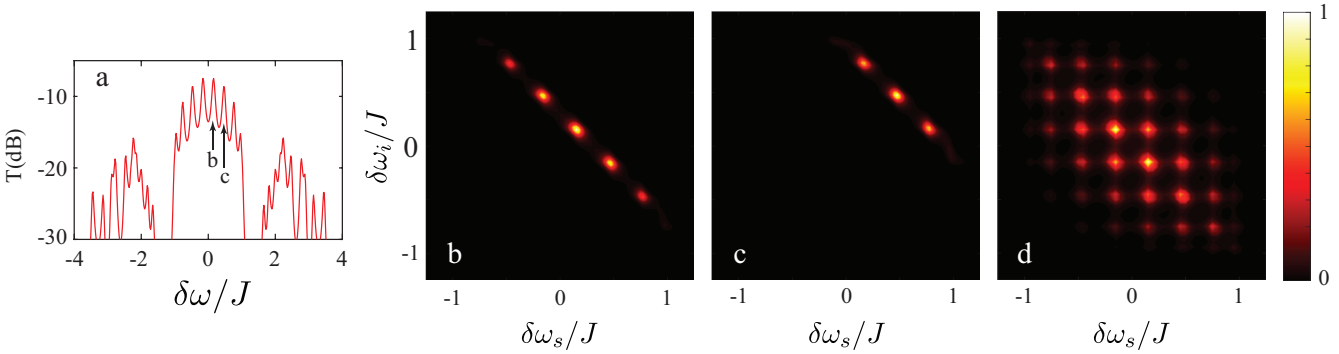

FIG. S8. **a** Simulated transmission spectrum of a device with $\kappa_{ex} = 0.1J$ showing individual edge mode resonances in the edge band. **b,c** Simulated JSI for narrow-band pump pulses, centered at edge state resonances, $(0.15J, 0.15J)$ and $(0.475J, 0.475J)$, respectively (indicated in **a**). The two-photon states in **b,c** are not separable. **d** Simulated JSI for broad-band pump pulses centered at $(0.15J, 0.15J)$ showing a nearly separable two-photon state.

S9: PAIR GENERATION RATES

An important parameter that characterizes a source of correlated photon pairs is the pair generation rate. Fig.S9 shows a comparison of the numerically simulated pair generation rates for a single-ring source (in the all-pass configuration) and a topological source (with 22 rings on the edge from input to the output port), as a function of the intrinsic loss rate κ_{in}/J. For these simulations we use equal pump powers and coupling rates $\kappa_{ex} = J$, and integrate the number of counts in a bandwidth of $2\kappa_{ex}$ around zero frequency detuning. We see that in the low loss regime ($\kappa_{in} < 0.05J$), a topological source can achieve an order of magnitude higher counts rates compared to a single ring source. This is because of the use of multiple ring resonators and the linear dispersion of the edge states, both of which enhance the pair generate rate. Therefore, pair generation rates can be enhanced even further by using bigger topological lattices. However, for higher κ_{in}, a topological source performs poorly because of the loss incurred in multiple ring resonators on the edge of the device. We note that for a given κ_{in}/J there is an optimal device size that yields maximum pair generation rate.

In our current experiment that uses silicon-on-insulator platform, the loss rate $\kappa_{in} \approx 1.3$ GHz and $J \approx 15$ GHz, which implies that our source is not operating in the low-loss regime. Nevertheless, by using low-loss platforms like silicon-nitride that are now commercially available [8], the loss rate κ_{in} can be reduced to below 100 MHz for similar values of J such that $\kappa_{in} < 0.01J$. Therefore, a low-loss realization of our topological source will significantly outperform a single-ring resonator source in terms of pair generation rate by an order of magnitude.

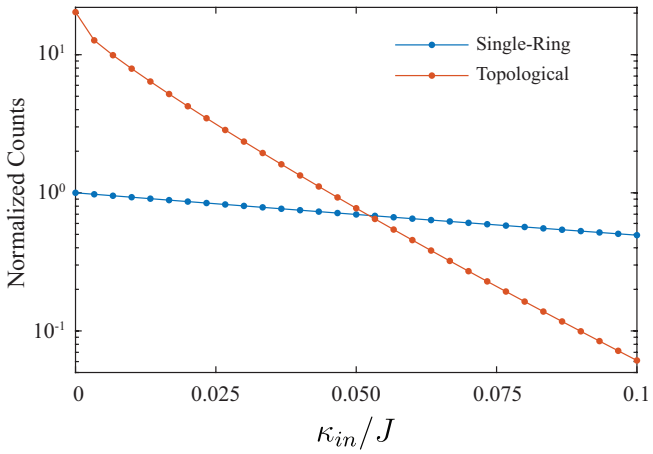

FIG. S9. Comparison of simulated photon-pair generation rates in a single-ring source and a topological source, as a function of the loss rate κ_{in}/J. The pair generation rate is normalized to that of a single-ring source with no loss.

S10: TUNABILITY OF SPECTRAL BANDWIDTH OF GENERATED PHOTONS

Figure S10 compares the tunability of the spectral bandwidth of generated photons in a topological source to that in a single-ring source (in the all-pass configuration), by tuning the two pump frequencies (indicated in the legend, in units of κ_{ex}). For a topological source, the full-width-half-max (FWHM) bandwidths of the generated photons are $\sim 1.4\kappa_{ex}$, $\sim 1\kappa_{ex}$, and $\sim 0.4\kappa_{ex}$, when the two input pump frequencies $(\omega_{p_1}, \omega_{p_2})$ are $(0,0)\kappa_{ex}$, $(0.4,0.4)\kappa_{ex}$, and $(0.8,0.8)\kappa_{ex}$, respectively. For a single-ring source, the FWHM bandwidths are $\sim 1.4\kappa_{ex}$, $\sim 1.6\kappa_{ex}$, and $\sim 2.3\kappa_{ex}$, when the input pump frequencies are $(0,0)\kappa_{ex}$, $(0.4,0.4)\kappa_{ex}$, and $(0.8,0.8)\kappa_{ex}$, respectively. For a topological source, we observe a reduction in the spectral bandwidth of generated photons by a factor of ~ 3.5 as we detune the pump frequencies further from the ring resonances. In contrast, for a single-ring source, the spectral bandwidth of the generated photons is more-or-less the same, and in fact, increases marginally when we significantly detune the pump frequencies away from the resonance. This is because, away from the resonance, the ring behaves as a waveguide with broad phase-matching with no resonant enhancement. Note that, for given input pump frequencies, the central frequencies of generated photons are constrained by the energy conservation relation, and are therefore, exactly the same in both the sources. Also, for the topological source, we assumed $J = \kappa_{ex}$.

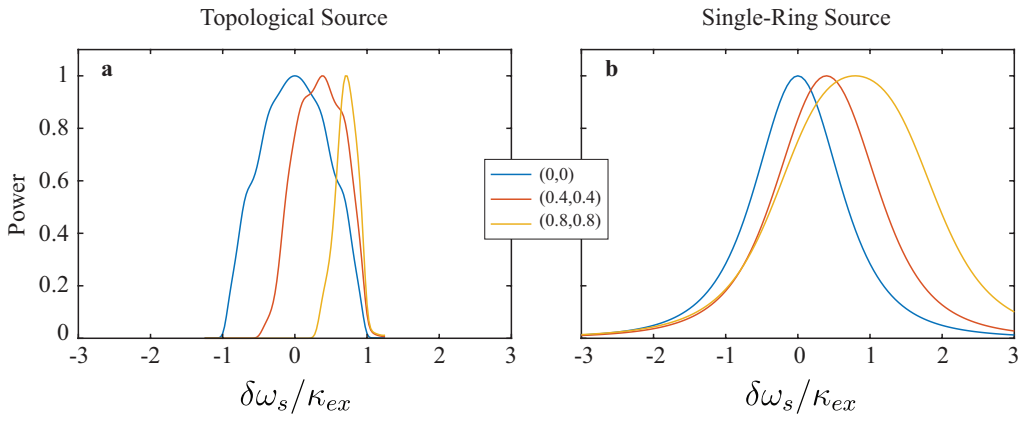

FIG. S10. Simulated spectra of the generated photons for different input pump frequencies (indicated on the figure, in units of κ_{ex}, for **a** a topological source, and **b** a single-ring source. The spectra are individually normalized to their maxima.

S11: SOURCE SPECTRUM

Our source operates in the telecom domain, near 1550 nm. A typical spectrum of photons generated by our source is shown in Fig.S11. This spectrum corresponds to the JSI measurements reported in Fig.2d of the main text.

[1] J. W. Silverstone, D. Bonneau, K. Ohira, N. Suzuki, H. Yoshida, N. Iizuka, M. Ezaki, C. M. Natarajan, M. G. Tanner, R. H. Hadfield, V. Zwiller, G. D. Marshall, J. G. Rarity, J. L. O'Brien, and M. G. Thompson, Nat. Photonics **8**, 104 (2013).
[2] J. Chen, K. F. Lee, and P. Kumar, Phys. Rev. A **76**, 031804 (2007).
[3] J. He, B. A. Bell, A. Casas-Bedoya, Y. Zhang, A. S. Clark, C. Xiong, and B. J. Eggleton, Optica **2**, 779 (2015).
[4] J. D. Franson, Phys. Rev. Lett. **62**, 2205 (1989).
[5] S. Mittal, E. A. Goldschmidt, and M. Hafezi, Nature **561**, 502 (2018).
[6] G. Harder and et.al., Opt. Express **21**, 13975 (2013).
[7] Z. Vernon, M. Menotti, C. C. Tison, J. A. Steidle, M. L. Fanto, P. M. Thomas, S. F. Preble, A. M. Smith, P. M. Alsing, M. Liscidini, and J. E. Sipe, Opt. Lett. **42**, 3638 (2017).
[8] Y. Zhang, M. Menotti, K. Tan, V. D. Vaidya, D. H. Mahler, L. Zatti, M. Liscidini, B. Morrison, and Z. Vernon, arXiv:2001.09474 (2020).

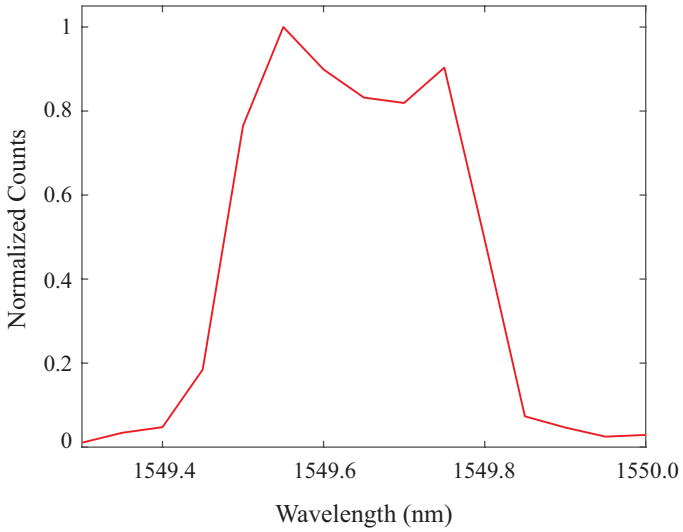

FIG. S11. Spectrum of generated photons, for the JSI measurements reported in Fig.2d of the main text.